Imaging Atomic Rearrangements in Two-Dimensional Silica Glass: Watching Silica's Dance

Pinshane Y. Huang,[1] Simon Kurasch,[2]* Jonathan S. Alden,[1]* Ashivni Shekhawat,[3] Alexander A. Alemi,[3] Paul L. McEuen,[3,4] James P. Sethna,[3] Ute Kaiser,[2] David A. Muller[1,4]†

Structural rearrangements control a wide range of behavior in amorphous materials, and visualizing these atomic-scale rearrangements is critical for developing and refining models for how glasses bend, break, and melt. It is difficult, however, to directly image atomic motion in disordered solids. We demonstrate that using aberration-corrected transmission electron microscopy, we can excite and image atomic rearrangements in a two-dimensional silica glass—revealing a complex dance of elastic and plastic deformations, phase transitions, and their interplay. We identified the strain associated with individual ring rearrangements, observed the role of vacancies in shear deformation, and quantified fluctuations at a glass/liquid interface. These examples illustrate the wide-ranging and fundamental materials physics that can now be studied at atomic-resolution via transmission electron microscopy of two-dimensional glasses.

Structural rearrangements play a key role in controlling the basic properties of glassy and disordered solids. Yet, studies of phenomena such as plastic deformation and phase change have been limited by the difficulty of tracking individual atoms in amorphous materials. As a result, many of the landmark studies on the atomic-scale underpinnings of these phenomena have been conducted by computer simulations (*1*–*5*) or with pseudo-atomic systems, such as micrometer-scale colloidal particles (*6*–*8*) or bubble-rafts (*9*), as stand-ins for atoms. To verify these findings, it is critical to develop experimental methods that can directly image the rearrangements of atoms in glasses. We demonstrate an approach to address this void: applying aberration-corrected high-resolution transmission electron microscopy (TEM) to image and restructure a two-dimensional (2D) silica glass (*10*, *11*). We first investigated the basic building blocks of plastic deformation by characterizing the strain around an isolated ring rearrangement. By comparing our experimental data with atomistic simulations, we show that, whereas the glass's structural disorder strongly affects its long-range elastic behavior, its short-range strain field resembles that of a crystal. Next, we investigated how multiple rearrangements interact to produce shear. We observed distinct, localized zones whose differing motions each contributed to the larger-scale deformation. Finally, we analyzed rearrangements at a sharp, but fluctuating, glass/liquid interface.

Two-dimensional silica is a layered polymorph of SiO_2. Its crystalline phase is a honeycomb lattice with an in-plane lattice constant $a = 5.4$ Å. Out-of-plane, it consists of two registered layers of SiO_4 tetrahedra (*10*, *12*). More interesting is the amorphous phase, shown in Fig. 1A and fig. S1. Amorphous 2D silica has an out-of-plane structure similar to that of its crystalline phase, but in-plane, it resembles the 2D continuous random network predicted by Zachariasen's model (*13*). Unlike typical 3D glasses, this 2D glass can be imaged at atomic resolution (*10*, *11*)—generating considerable recent interest (*14*–*16*). Both phases can be synthesized in a chemical vapor deposition (CVD) furnace (*10*, *17*) or grown by molecular beam epitaxy on metal substrates (*11*, *12*). For this work, we used CVD-grown silica supported on a graphene substrate (*17*) from the same batch of samples as discussed in (*10*). The graphene serves as a mostly transparent, chemically inert imaging substrate (*18*, *19*).

To image and induce atomic motion in the 2D silica, we used low-voltage, aberration-corrected high-resolution TEM at 80 kV. Similar techniques have been used to visualize structural transformations such as molecular motions (*20*) and rearrangements in 2D crystals such as graphene (*21*–*26*). The electron beam produces broad-beam illumination (~100 nm in diameter) with typical dose rates of ~1.4×10^6 electrons/nm^2 s and frame rates of ~1 to 2 s. With low probabilities, electrons can transfer sufficient local energy to eject atoms or break bonds through elastic or inelastic scattering (*27*–*30*). These processes result in mobile (mainly oxygen) vacancies, which produce strain and enable plastic deformation, flow, and even local melting well below the glass transition temperature (*27*–*30*). For large atom displacements (>1 bond length) that change the local bonding configuration, we observed on the order of ~10^{-4} displacements/nm^2 s in the bulk, or roughly one displacement every several images. Because these large atom displacements are relatively rare, we could use the electron beam both as a source for randomly induced structural rearrangements and as a probe to track the material's response.

These techniques produced videos of restructuring, such as the isolated ring rearrangement shown in Fig. 1, B to E, and corresponding movie S1. Such rearrangements are worth examining in detail because they are the building blocks of plastic deformation. Figure 1B shows a high-resolution TEM image of a small region of 2D silica with a cluster of rings initially arranged in a 5-7-5-7 configuration. Each dark spot in the image represents the location of one structural unit: two stacked SiO_4 tetrahedra that are registered out-of-plane. As we continued imaging (Fig. 1, C to E), the 5-7-5-7 cluster transformed into a 6-6-6-6 cluster. Surprisingly, the transformation occurred over several frames. In the 12 s between the stable initial and final configurations, we observed several metastable intermediate states. A similar transformation has been modeled in (*11*).

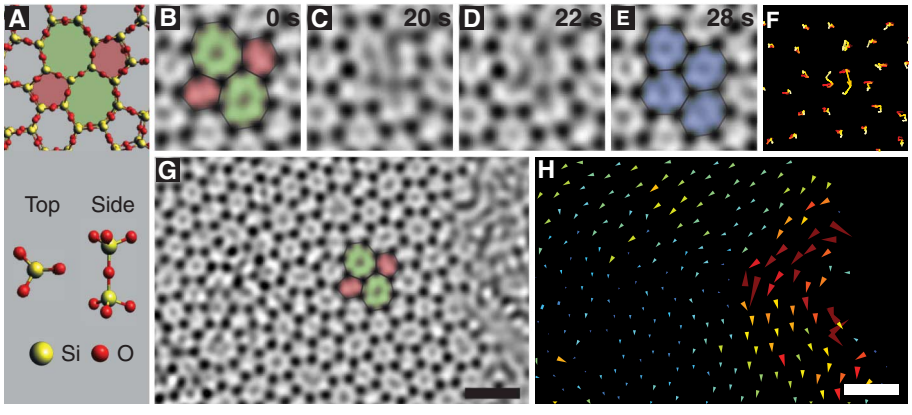

Fig. 1. Elastic and plastic deformation in ring exchange. (**A**) Cartoon models of the 2D silica structure. (**B** to **E**) TEM images showing a ring rearrangement that transforms a 5-7-5-7 cluster into a 6-6-6-6 cluster. The dark spots are Si-O-Si columns that correspond with the top and side views in (A). Images have been smoothed and Fourier-filtered to remove the graphene lattice background [see figs. S2 and S3 and (*17*)]. (**F**) A trajectory map of the atomic sites. Color (red to yellow) indicates time of motion. (**G**) Larger view of the region from (A), and (**H**) corresponding first-to-last frame displacement map. The arrows have been enlarged ×2 to increase visibility; color indicates size of displacement, from 0 (dark blue) to ≥1.3 Å (red). The region between the bond rearrangement and the edge of the sheet exhibits strong local rotation. Scale bars: 1 nm. See also movies S1 and S2.

[1]School of Applied and Engineering Physics, Cornell University, Ithaca, NY 14853, USA. [2]Electron Microscopy Group of Materials Science, University of Ulm, Ulm 89081, Germany. [3]Laboratory of Atomic and Solid State Physics, Cornell University, Ithaca, NY 14853, USA. [4]Kavli Institute at Cornell for Nanoscale Science, Cornell University, Ithaca, NY 14853, USA.

*These authors contributed equally to this work.
†Corresponding author. E-mail: dm24@cornell.edu

We tracked the position of the atoms over time to measure elastic and plastic deformation in the glass. Each line in Fig. 1F represents the trajectory of a single atomic site in Fig. 1, B to E. We produced these trajectories by cross-correlating our images to remove net motion, fitting Gaussians at each atomic site, and then tracking the atoms from frame to frame using particle-tracking software adapted from colloids research (*17*, *31*). Because 2D silica contains two registered layers of SiO_4 tetrahedra and because Si atoms dominate the TEM image contrast, our methods effectively track the in-plane motion of Si pairs. The two trajectories in the center of Fig. 1F represent plastic deformation: atomic sites that break and form new bonds. We also see the small motions of nearby atoms that move relative to one another while retaining their nearest-neighbor bonding; these are elastic deformations.

The elastic motion of atoms around the ring rearrangement is pronounced on larger length scales. Figure 1G shows an overview image of the bond rearrangement and its proximity to the edge of the silica sheet (right-hand side) (see also movies S1 and S2). Figure 1H shows the corresponding displacement vector field from the first to last frames, a time frame of $\Delta t = 28$ s. The displacement field is dominated by a strong local rotation in the region between the ring exchange and the edge of the sheet.

We examined the correlation between elastic and plastic deformations by analyzing the short-range elastic behavior, as shown in Fig. 2, A to H. Using our tracking data, we took the spatial derivative of the displacement field. This produced the displacement gradient field, which could be separated into its symmetric component, the 2D strain tensor $\boldsymbol{\varepsilon}$, and its antisymmetric component, the local rotation matrix $\boldsymbol{\omega}$ (*32*). We plot the magnified, independent experimental components of $\boldsymbol{\varepsilon}$ and $\boldsymbol{\omega}$ in Fig. 2, A to D. These components respectively represent the local volume change, shear, and local rotation. In this analysis, the motion of the two middle atoms has been removed to isolate the elastic behavior.

To understand these strain components, we conducted molecular dynamics simulations of the ring exchange using the large-scale atomic/molecular massively parallel simulator (LAMMPS) (*17*, *33*). We first produced relaxed structures of 2D silica crystals embedded with either a 5-7-5-7 or 6-6-6-6 cluster. These structures simulate our before-and-after atom configurations and can be processed with the same methods as our experimental images. The resulting $\boldsymbol{\varepsilon}$ and $\boldsymbol{\omega}$ components are shown in Fig. 2, E to H. The agreement between our simulations and experiment provides evidence that our observed elastic displacements are directly correlated to the plastic deformation of the ring exchange and likely represent the relaxation of the structure around the new ring configuration. Our experimental strain fields also match those of an elastic dipole (*34*), suggesting that even at the atomic scale, continuum elastic mechanics can provide a good model for atomic rearrangements (fig. S4). Finally, the agreement between (amorphous) experiment and (crystalline) simulation suggests that on very short length scales (<1.5 nm), the elastic response of the amorphous material is similar to that of a crystal—in much the same way that the short-range order of amorphous and crystalline materials are also similar.

On larger length scales, however, the elastic deformation of our system deviates from that of an infinite crystal. Figure 2, I to L, shows LAMMPS simulations of displacement fields for a 5-7-5-7 to 6-6-6-6 ring exchange representing four cases: a crystal (Fig. 2I), an amorphous sheet (Fig. 2J), and crystalline and amorphous sheets with an edge (Fig. 2, K and L). These plots separate the key effects contributing to the experimental behavior seen in Fig. 1H. The "crystal" simulation in Fig. 2I displays a highly symmetric displacement field that lacks agreement with our experimental data. In Fig. 2J, adding structural disorder to simulate an "amorphous" structure damps the symmetry of the strain field and improves agreement with experiment. In Fig. 2, K and L, adding an edge strongly enhances the displacements between the ring exchange and the edge. Figure 2L yields qualitative agreement with the experimental results in Fig. 1H.

In crystals, plastic deformation frequently occurs by introducing and migrating dislocations through the lattice. For amorphous materials, however, this process is far less well understood. One model proposes that deformation in amorphous materials is mediated by shear transformation zones—concentrated, local regions of shear strain that rearrange and interact to produce net deformation (*1*, *4*, *6*). Shear transformation zones have been directly observed in colloidal glasses and have been proposed as a model for metallic glasses (*6*).

Figure 3A shows atomic trajectories in a region undergoing shear, shown in Fig. 3B (see also fig. S5 and movie S3). Shear deformation is apparent when comparing the trajectories of atomic sites in region 1 (top left) and region 3 (bottom right). Although most atoms in region 1 oscillate near their original positions (highlighted in the enlarged atom trajectory and before-and-after bond configuration in Fig. 3C), the atoms in region 3 collectively displace by ~2.4 Å relative to region 1 (Fig. 3D). The mechanisms enabling this displacement are visible in regions 2 and 4, which separate the two displacing regions. Both regions 2 and 4 contain a large number of ring rearrangements; one isolated example is shown in Fig. 3E. These rearrangements appear to be mediated by nearby defects: Region 4 is at the edge of the solid, whereas region 2 contains a handful of vacancies (arrows in Fig. 3B). Over the course of the video, this vacancy-induced restructuring gradually changes the bonds connecting regions 1 and 3, enabling their relative displacement. Although the uniform electron beam cannot directly apply shear forces, possible sources of shear stress include forces applied from the edge

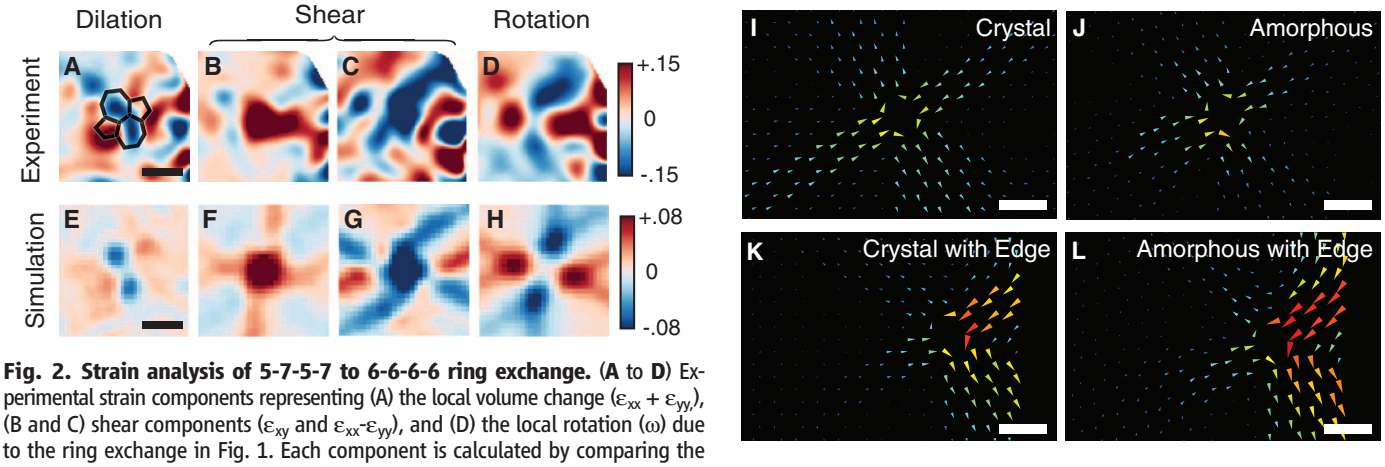

Fig. 2. Strain analysis of 5-7-5-7 to 6-6-6-6 ring exchange. (**A** to **D**) Experimental strain components representing (A) the local volume change ($\varepsilon_{xx} + \varepsilon_{yy}$), (B and C) shear components (ε_{xy} and ε_{xx}-ε_{yy}), and (D) the local rotation (ω) due to the ring exchange in Fig. 1. Each component is calculated by comparing the position of atoms between the first and last frames, excluding the two atoms at the center of the bond exchange to isolate elastic behavior (*17*). Overlaid polygons show the original ring configuration. Scale bars: 1 nm. (**E** to **H**) LAMMPS simulations for the 5-7-5-7 to 6-6-6-6 ring exchange in crystalline 2D silica. (**I** to **L**) Simulated displacement maps isolating the effects of structural and edge disorder. Arrows have been enlarged ×4 for visibility. Color scale is from 0 (dark blue) to ≥1 Å (red). Scale bars: 1 nm.

of the sheet by the surrounding material, interactions with the graphene substrate, or internal strain in the disordered silica. Our observation of localized regions of large rearrangements suggests a covalently bonded molecular glass analog for the shear transformation zones seen in other glassy systems.

Figure 4 shows a third class of dynamics that we studied, the rearrangements of atoms at the edge of the 2D sheet. One common way to distinguish solids and liquids is their behavior under stress. Under stress, typical solids exhibit first a linear strain in the elastic regime, followed by a nonlinear stress-strain curve in the plastic regime. This onset of nonlinearity reflects, in part, the activation energy to form and migrate dislocations in crystals, or to nucleate similar rearrangements such as shear transformations in amorphous solids. These rearrangements produce long-range strain fields. In these respects, the rearrangements observed in the glassy 2D silica discussed above typify the behavior of solids under stress.

In addition to these "solid-like" behaviors that we observed in our 2D glassy phase, we also observed the formation of a second phase, highlighted in blue. This phase is distinguished by its fast mean atomic displacements (>1 bond length between frames) under the electron beam. Importantly, because of its fast rearrangement time scales, this phase is "liquid-like" on the imaging time scales: Under the effective heat bath of the electron beam, it rearranges too quickly to support stresses. These characteristics make our system a nonequilibrium analogy to the equilibrium solid-liquid interface. Electron energy loss spectroscopy confirms that this second phase is composed of oxygen-deficient silica, which has been shown to rearrange more quickly under electron irradiation than stoichiometric SiO_2 (*28*). Structurally, this material may be composed of rapidly rearranging 3D amorphous silicon suboxide, monotetrahedral layers of silica, out-of-plane mismatched bitetrahedral layers, or combinations thereof. The structure of this interface is unusual: It resembles neither the sharp, faceted surfaces at crystal/liquid interfaces (*35*, *36*) reported in the literature, nor the gradual evolution in properties that are typical in thermally driven glass/liquid transitions (*7*, *8*). The transition between the two phases occurs over ~1 nm (Fig. 4A, on the blue side of the interface).

Figure 4, A to D, shows the time evolution of the interface. In Fig. 4, B to D, "solid-like" regions that have undergone the most displacement relative to their initial configurations are highlighted in red (*17*). The fastest-moving atoms are concentrated near the edge of the sheet in each frame; here, large sections dissociate and re-form several times over the course of the video, producing new arrangements and sizes of rings with no apparent memory of the previous state. Figure 4E plots the mean squared displacement of atoms in the solid, which increases markedly with proximity to the edge of the sheet for all time intervals measured. This increased motion consists of both increased elastic motion and bond rearrangements of atoms near the edge. An increase in mean displacements at solid/liquid interfaces has also been observed in hard-sphere colloids (*37*). During the video, the area of the solid and length of the interface fluctuate without increasing or decreasing measurably (fig. S6 and movies S4 and S5), indicating that we are observing the sample near a steady state rather than simply damage-related degradation of the solid.

We have demonstrated a promising avenue for understanding the structure and dynamics of glasses through atomic resolution imaging of 2D glasses. Future work that combines these techniques with well-defined in situ stimuli, such as heating, straining, and electrical biasing, should further extend the potential of these techniques, making it possible to correlate microscopic rearrangements with bulk thermodynamic properties.

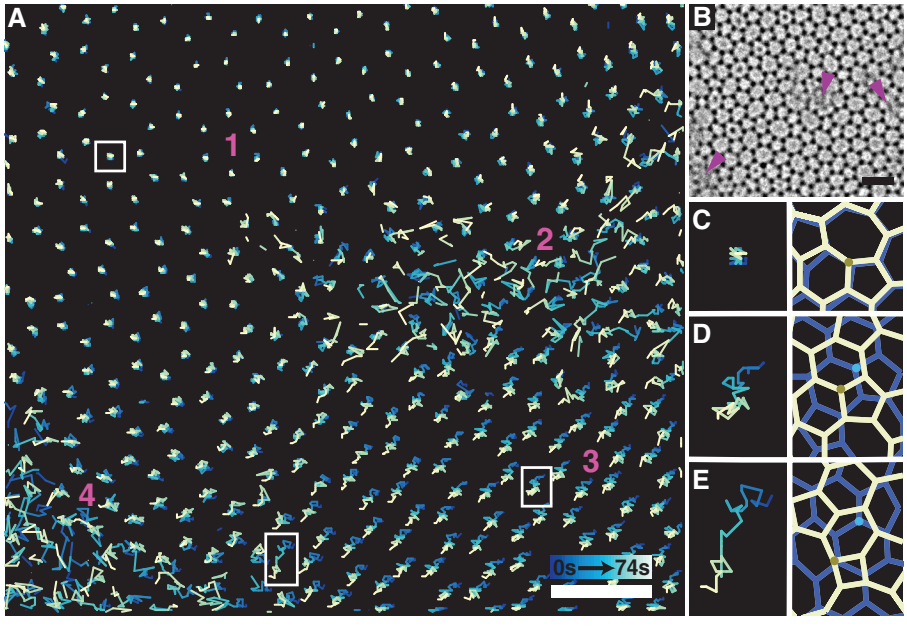

Fig. 3. Imaging and trajectories of shear deformation. (**A**) Trajectory map over 74 s. The original image is shown in (**B**), where purple arrows indicate vacancies. The trajectories show four regions with distinct types of motion: oscillation around initial positions (region 1), gradual displacement by ~2.4 Å (region 3), and ring rearrangements near vacancies (region 2) or at the edge of the sheet (region 4). The shear strain and bond rearrangements appear directly related: The restructuring in regions 2 and 4 changes the bonds connecting regions 1 and 3, enabling their relative displacement. (**C** to **E**) Magnified trajectories (left) and before-and-after bonding configurations (right). (C) oscillates near its original position; (D) moves under shear; and (E) undergoes bond rearrangement. See also movie S3. Scale bars: 2 nm.

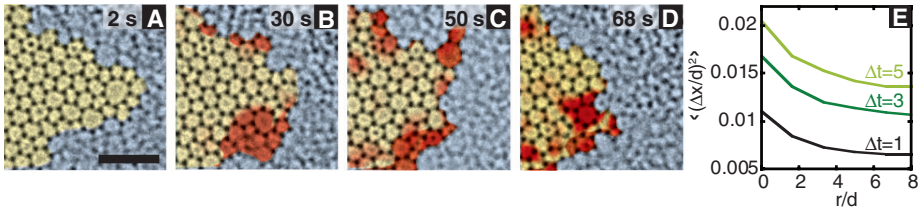

Fig. 4. Restructuring at the edge of the 2D silica sheet. (**A** to **D**) Image series of interfacial restructuring. The solid phase is false-colored yellow, with red highlighting the regions of largest rearrangement relative to the first frame (*17*). The "liquid-like" phase is colored blue. Scale bar: 2 nm. See also movies S4 and S5. (**E**) Mean squared displacement $\langle|\Delta x/d|^2\rangle$ of "solid" atoms versus their distance r from the edge for time intervals of Δt = 1, 3, and 5 s. Both axes are normalized by d, the mean in-plane Si-Si spacing. Atoms near the edge move faster than atoms in the bulk.

References and Notes

1. M. L. Falk, J. S. Langer, *Phys. Rev. E* **57**, 7192–7205 (1998).
2. K. Maeda, S. Takeuchi, *Phys. Status Solidi* **49**, 685–696 (1978) (a).
3. M. L. Falk, C. E. Maloney, *Eur. Phys. J. B* **75**, 405–413 (2010).
4. M. L. Manning, J. S. Langer, J. M. Carlson, *Phys. Rev. E* **76**, 056106 (2007).
5. H. He, M. F. Thorpe, *Phys. Rev. Lett.* **54**, 2107–2110 (1985).
6. P. Schall, D. A. Weitz, F. Spaepen, *Science* **318**, 1895–1899 (2007).
7. W. K. Kegel, A. von Blaaderen, *Science* **287**, 290–293 (2000).
8. E. R. Weeks, J. C. Crocker, A. C. Levitt, A. Schofield, D. A. Weitz, *Science* **287**, 627–631 (2000).
9. A. S. Argon, H. Y. Kuo, *Mater. Sci. Eng.* **39**, 101–109 (1979).
10. P. Y. Huang *et al.*, *Nano Lett.* **12**, 1081–1086 (2012).
11. L. Lichtenstein *et al.*, *Angew. Chem. Int. Ed.* **51**, 404–407 (2012).

12. D. Löffler *et al.*, *Phys. Rev. Lett.* **105**, 146104 (2010).
13. W. H. Zachariasen, *J. Am. Chem. Soc.* **54**, 3841–3851 (1932).
14. L. Lichtenstein, M. Heyde, H.-J. Freund, *Phys. Rev. Lett.* **109**, 106101 (2012).
15. M. Wilson, A. Kumar, D. Sherrington, M. F. Thorpe, *Phys. Rev. B* **87**, 214108 (2013).
16. F. Ben Romdhane *et al.*, *ACS Nano* **7**, 5175–5180 (2013).
17. Materials and methods are available as supplementary materials on *Science* Online.
18. Z. Lee *et al.*, *Nano Lett.* **9**, 3365–3369 (2009).
19. R. S. Pantelic, J. C. Meyer, U. Kaiser, H. Stahlberg, *Solid State Commun.* **152**, 1375–1382 (2012).
20. E. Nakamura, *Angew. Chem. Int. Ed.* **52**, 236–252 (2013).
21. A. Hashimoto, K. Suenaga, A. Gloter, K. Urita, S. Iijima, *Nature* **430**, 870–873 (2004).
22. J. C. Meyer *et al.*, *Nano Lett.* **8**, 3582–3586 (2008).
23. J. H. Warner *et al.*, *Science* **337**, 209–212 (2012).
24. J. Kotakoski *et al.*, *Phys. Rev. B* **83**, 245420 (2011).
25. J. Kotakoski, A. V. Krasheninnikov, U. Kaiser, J. C. Meyer, *Phys. Rev. Lett.* **106**, 105505 (2011).
26. S. Kurasch *et al.*, *Nano Lett.* **12**, 3168–3173 (2012).
27. S. G. Mayr, Y. Ashkenazy, K. Albe, R. S. Averback, *Phys. Rev. Lett.* **90**, 055505 (2003).
28. K. Zheng *et al.*, *Nature Communications* **1**, 24 (2010).
29. L. W. Hobbs, M. R. Pascucci, *J. Phys. Colloq.* **41**, C6-237–C6-242 (1980).
30. P. M. Ajayan, S. Iijima, *Philos. Mag. Lett.* **65**, 43–48 (1992).
31. J. C. Crocker, D. G. Grier, *J. Colloid Interface Sci.* **179**, 298–310 (1996).
32. B. A. Auld, *Acoustic Fields and Waves in Solids* (Wiley, New York, 1973).
33. S. Plimpton, *J. Comput. Phys.* **117**, 1–19 (1995).
34. E. R. Grannan, M. Randeria, J. P. Sethna, *Phys. Rev. B* **41**, 7784–7798 (1990).
35. J. M. Howe, H. Saka, *MRS Bull.* **29**, 951–957 (2004).
36. S. E. Donnelly *et al.*, *Science* **296**, 507–510 (2002).
37. J. Hernández-Guzmán, E. R. Weeks, *Proc. Natl. Acad. Sci. U.S.A.* **106**, 15198–15202 (2009).

Acknowledgments: The raw data presented in this work are available in the supplementary movies. S.K. acquired, aligned, and preprocessed the TEM data under the supervision of U.K. P.Y.H. and J.S.A. designed and conducted the atom tracking and strain and deformation analysis under the supervision of D.A.M. and P.L.M. A.S., A.A.A., and J.P.S. contributed theoretical understanding via continuum mechanics analysis and LAMMPS simulations. P.Y.H., J.S.A, and D.A.M. wrote the paper. All authors contributed to the discussion of results and commented on and edited the paper. This work was supported by the NSF through the Cornell Center for Materials Research (NSF DMR-1120296). Additional support for P.Y.H. was provided by the NSF Graduate Research Fellowship Program under grant DGE-0707428. A.A.A., A.S., and J.P.S. were supported by NSF grant PHY-0941095. J.S.A. and P.L.M were supported by the Air Force Office of Scientific Research through the Graphene MURI (FA9550-09-1-0691 and FA9550-10-1-0410). U.K. and S.K. acknowledge support from the Deutsche Forschungsgemeinschaft (German Research Foundation) and the Ministry of Science, Research and the Arts (MWK) of Baden-Württemberg through the Sub Angstrom Low-Voltage Electron Microscopy project. The authors acknowledge discussions with M. K. Blees, I. Cohen, S. J. Gerbode, R. Hovden, J. Kotakoski, A. V. Krasheninnikov, B. Leahy, Y.-C. Lin, M. L. Manning, E. R. Weeks, and A. M. van der Zande. We thank A. Srivastava, V. Skakalova, and J. Smet from the Max Planck Institute for Solid State Research in Stuttgart, Germany, for the sample. Microscopy support and maintenance were provided by J. Biskupek.

Supplementary Materials
www.sciencemag.org/content/342/6155/224/suppl/DC1
Materials and Methods
Figs. S1 to S6
Movies S1 to S5
References (*38*–*40*)

21 June 2013; accepted 26 August 2013
10.1126/science.1242248

Waveform Tomography Reveals Channeled Flow at the Base of the Oceanic Asthenosphere

Scott French,[1] Vedran Lekic,[2] Barbara Romanowicz[1,3,4]*

Understanding the relationship between different scales of convection that drive plate motions and hotspot volcanism still eludes geophysicists. Using full-waveform seismic tomography, we imaged a pattern of horizontally elongated bands of low shear velocity, most prominent between 200 and 350 kilometers depth, which extends below the well-developed low-velocity zone. These quasi-periodic fingerlike structures of wavelength ~2000 kilometers align parallel to the direction of absolute plate motion for thousands of kilometers. Below 400 kilometers depth, velocity structure is organized into fewer, undulating but vertically coherent, low-velocity plumelike features, which appear rooted in the lower mantle. This suggests the presence of a dynamic interplay between plate-driven flow in the low-velocity zone and active influx of low-rigidity material from deep mantle sources deflected horizontally beneath the moving top boundary layer.

Mantle convection is responsible for driving plate motions on Earth, but the detailed morphology of convection patterns remains unresolved. Because seismic velocities are affected by temperature, and seismic anisotropy is affected by alignment of crystals, seismic tomography can be used to map the patterns of flow in the earth's mantle. Global seismic mantle tomography has provided important constraints on the long-wavelength shear-velocity structure, highlighting in particular the correlation of velocity patterns in the top 200 km with surface tectonics and documenting the widespread presence of the low-velocity zone (LVZ) under ocean basins. Likewise, the presence of two antipodal large low-shear-velocity provinces (LLSVPs) at the base of the mantle under the central Pacific and Africa is a robust feature of all tomographic models (*1*). Hotspots appear to be located preferentially above the LLSVPs (*2*) or on their borders (*3*). There is also a striking correlation at long wavelengths between the location of the LLSVPs and high attenuation in the mantle transition zone (*4*). However, plume conduits (*5*, *6*) and roll-like secondary convection patterns (*7*) remain difficult to image tomographically.

We used full-waveform inversion, coupled with synthetic seismogram computation using the Spectral Element Method, to image global radially anisotropic shear-velocity (V_S) structure at upper-mantle and transition-zone depths. This approach is well suited to remedy the known limitations of classical tomographic techniques (*8*), as already demonstrated at the local (*9*) and regional (*10*) scales. Our second-generation global model, SEMum2, refines an earlier one developed by our group (*11*) and in particular includes a more realistic crust (supplementary text and figs. S1 to S4). Compared with other global shear-velocity models (figs. S5 to S8), SEMum2 more accurately recovers both the depth and strength of the low-velocity minimum under ridges. It also shows stronger velocity minima in the LVZ, a more continuous signature of fast velocities in subduction zones, and stronger, clearly defined, low-velocity "conduits" under the Pacific Superswell (*12*) while confirming the robust long-wavelength structure imaged in previous studies (supplementary text S2.3 and figs. S7 and S8), such as the progressive weakening and deepening of the oceanic LVZ with overlying plate age.

Cluster analysis (*13*) of V_S profiles in the depth range 30 to 350 km in SEMum2 (supplementary text S3) provides an objective way to analyze the model and isolates an anomalously low-velocity region—most prominent in the depth range 200 to 350 km although also reflected in the overlying LVZ (Fig. 1, A and B, and fig. S9), organized in elongated bands, and clearest on the Pacific plate (Fig. 1A), where it spans from ~100 million-year-old ocean floor to the East Pacific Rise (EPR). In a map view of SEMum2 at a depth of 250 km (Fig. 2A), these prominent structures appear as fingerlike zones of significantly slower-than-average V_S (~3 to 4%). They are also present under other plates: off west Antarctica, in some parts of the North and South Atlantic and western Indian Oceans, and possibly in the southwestern part of the Australian plate (Fig. 2A and fig. S10). These fingerlike structures are not only well-resolved in the SEMum2 model but also are robust with respect to estimated model uncertainties, are compatible with independent waveform data, and cannot be explained by unmapped azimuthal anisotropy in our inversion (supplementary text S4 and figs. S13 to S17).

[1]Berkeley Seismological Laboratory, 209 McCone Hall, Berkeley, CA 94720, USA. [2]Department of Geology, University of Maryland, College Park, MD 20742, USA. [3]Collège de France, 11 Place Marcelin Berthelot, 75005 Paris, France. [4]Institut de Physique du Globe de Paris, 1 rue Jussieu, 752382 Paris Cedex 05, France.
*Corresponding author. E-mail: barbara@seismo.berkeley.edu